Received: 28 January 2019 | Revised: 31 March 2019 | Accepted: 1 April 2019

DOI: 10.1002/er.4580

RESEARCH ARTICLE

WILEY INTERNATIONAL JOURNAL OF ENERGY RESEARCH

Radioluminescent nuclear battery containing $CsPbBr_3$ quantum dots: Application of a novel wave-shifting agent

Wang Chen | Xiaobin Tang | Yunpeng Liu | Zhiheng Xu | Yuan Zicheng | Zhengrong Zhang | Kai Liu

Department of Nuclear Science and Engineering, Nanjing University of Aeronautics and Astronautics, Nanjing 211106, China

Correspondence
Xiaobin Tang, Department of Nuclear Science and Engineering, Nanjing University of Aeronautics and Astronautics, Nanjing 211106, China.
Email: tangxiaobin@nuaa.edu.cn

Funding information
National Natural Science Foundation of China, Grant/Award Number: 11675076; Shanghai Aerospace Science and Technology Innovation Project, Grant/Award Number: SAST2016112

Summary

Radioluminescent nuclear battery has been widely studied for its miniaturization and long life. In this study, all-inorganic perovskite quantum dots ($CsPbBr_3$ QDs) were selected as a novel wave-shifting agent combined with liquid scintillator PPO (2,5-diphenyloxazole). The QDs were used to regulate the emission spectrum to match different GaAs devices. The maximum output power of the RL nuclear battery was greatly enhanced by 1.91 to 2.53 times. Perovskite QDs with adjustable emission spectra were used as wave-shifting agents and exhibited more excellent properties and application prospects than traditional wave-shifting agents. The Monte Carlo method was used to simulate the energy deposition of fluorescent materials under various radioactive source models. Results verified the advantages of using liquid radioactive sources and liquid fluorescent materials. The application and reference value of perovskite QDs in nuclear detection and nuclear medical imaging were also discussed.

KEYWORDS

Monte Carlo simulation, perovskite quantum dots, RL nuclear battery, spectral regulation, wave-shifting agent

1 | INTRODUCTION

For deep space exploration, nuclear batteries have become the inevitable choice because of their long-term stability of power supply,[1,2] unaffected by the external environment, long service life,[3,4] safety, and reliability.[5,6]

Radioluminescent (RL) nuclear batteries can be miniaturized[7,8] and have been extensively studied. Radioluminescent nuclear battery is a kind of indirect energy-conversion nuclear battery; the RL nuclear battery consists of radiation sources, fluorescent materials, and photovoltaic cells. The indirect energy conversion mode can effectively reduce the radiation damage effect of the energy conversion unit in the device. This energy conversion method is expected to be applied to radiation sources with high activity and energy density.[9,10]

Previous research works mainly focused on revealing the influencing factors of RL nuclear battery and improving the property of electrical output.

The specific research work on RL nuclear battery mainly includes selecting energy exchange materials, adjusting physical parameters,[11-13] optimizing structural design,[14,15] and analyzing service environment.[16,17] The results show that the output performance of nuclear battery can be effectively improved by choosing excellent fluorescent and semiconductor energy conversion materials, optimizing structural design, and improving the service environment of nuclear battery. In the previous research, we found that by selecting the fluorescent materials which can achieve spectral regulation to match photovoltaic semiconductor, we can obtain better electrical performance.[18]

Fluorescent materials with adjustable emission spectrum have been explored to optimize their matching of fluorescent materials and energy conversion devices, regulate the emission spectrum to match those of the devices, and ultimately, improve the overall electrical property of nuclear batteries.[19]

Perovskite quantum dots (QDs) and traditional QDs have developed rapidly in the fields of LED, solar cells, and sensors. Kovalenko et al[18] reported that $CsPbX_3$ (X = Cl, Br, and I) QDs exhibit approximately 90% photoluminescence (PL) efficiency, which is superior to those of CdSe-based QDs even after surface modification. Due to the unique and excellent optical properties of quantum dots, the research on the radioluminescence of quantum dots has been reported successively.[20-23]

In this study, selective perovskite QDs with excellent luminescence properties were used to control the emission spectra of conventional fluorescent materials. The main research method included the characterization of QD fluorescent materials, evaluation of the optical and electrical properties of the RL nuclear battery after spectral regulation and the gain of the electrical properties, and calculation of the adaptation factors for different devices after the spectrum regulation. Monte Carlo method was used to simulate the absorption dose and energy deposition of the fluorescent materials by using various radiation source models. The variation in energy deposition in the various radiation source models and various physical parameters was studied. The applicability and significance of the optimization of devices in nuclear detection and nuclear medical imaging were also discussed. Figure 1 presents the physical diagram of the QD/PPO RL nuclear battery and the schematic diagram of the QD spectral regulation process.

Highlights

- The application of $CsPbBr_3$ quantum dots as wave-shifting agents in RL nuclear batteries and the performance comparison of POPOP are first reported.
- $CsPbBr_3$ quantum dots successfully regulated the RL spectrum of PPO and obtained 3.30 to 3.35 times optical property.
- $CsPbBr_3$ quantum dot eventually increased the maximum output power of RL nuclear batteries by 1.91 to 2.53 times, and the gain effect was better than POPOP.
- Using the advantages of quantum dot spectrum regulation and liquid fluorescent materials, the design scheme of 1.15-μW RL nuclear batteries was obtained by MCNP simulation calculation, which greatly improved the output power of RL nuclear batteries.

2 | MATERIALS AND METHODS

2.1 | Synthesis and characterization of $CsPbBr_3$ QDs

$CsPbBr_3$ QDs were synthesized by hot injection with oleylamine and oleic acid as surfactant. Surface alkyl promoted the dispersion of $CsPbBr_3$ QDs in an organic solvent. In brief, 20 mg of PPO powder was added into 10 mL of the QD solution and magnetically stirred until fully dissolved to obtain $CsPbBr_3$ QD/PPO solution. The mass concentrations of the QD/PPO and QD solutions configured in this paper are 10 mg/mL POPOP/PPO solution. The solution was prepared by adding 0.2 mg of POPOPO and 20 mg of PPO powder into 10 mL of toluene solution followed by magnetic stirring until fully dissolved. (synthesis details were represented in the Supporting Information).

To characterize $CsPbBr_3$ QDs, we used high-resolution transmission electron microscope (HRTEM). Figure 2A-C shows that monodisperse $CsPbBr_3$ QDs have a particle sizes of 7.38 nm and a cubic shape. The conventional optical properties of the $CsPbBr_3$ QDs were characterized by recording the PL and Abs spectra. Figure 1E shows the typical ultraviolet-visible (UV-Vis) absorption and PL spectra of the $CsPbBr_3$ QDs. The $CsPbBr_3$ QDs exhibited strong PL with a central wavelength of 512.9 nm and a narrow full width at half-maximum (FWHM) of 12.1 nm. The sharp absorption edge is located at 460 to 500 nm.

2.2 | Determination of the optimal concentration of $CsPbBr_3$ QDs

Previous work proved the RL effect of $CsPbBr_3$ QDs.[20] We selected traditional liquid scintillator PPO and $CsPbBr_3$ QDs as the fluorescent materials for RL nuclear battery. PPO was dissolved in toluene, to obtain different solution concentrations (1-6 mg/mL) for measuring RL intensity under a fixed tube voltage of a 60 kV and tube current of 800 μA. The optimum concentration of the solute in the PPO and POPOP/PPO solutions was finally determined (Figures S1 and S2). In brief, 20 mg of PPO powder was added into 10 mL of the QD solution and magnetically stirred until fully dissolved to obtain $CsPbBr_3$

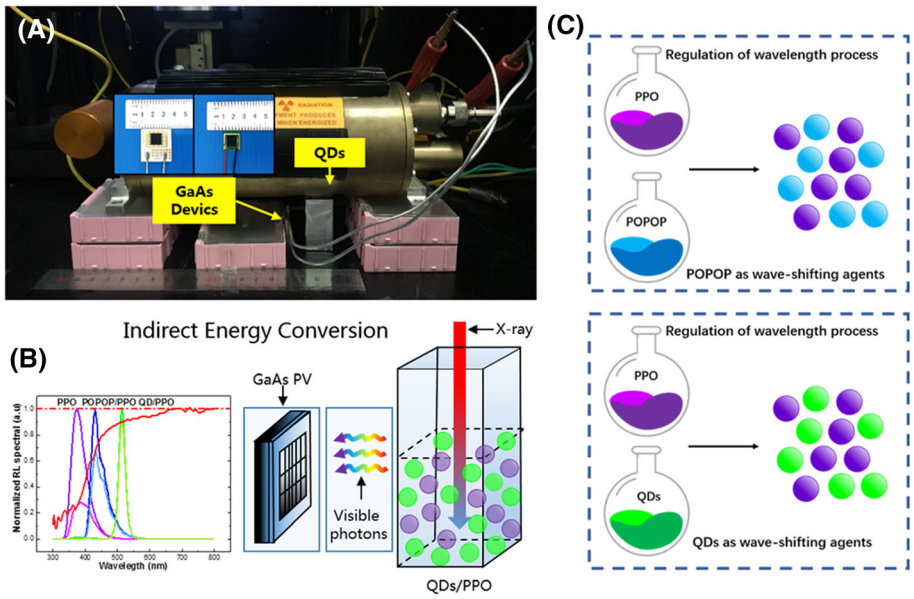

FIGURE 1 A, Physical and B, schematic diagrams of the QD/PPO RL nuclear battery; and C, schematic diagram of POPOP and $CsPbBr_3$ QDs spectral regulation processes [Colour figure can be viewed at wileyonlinelibrary.com]

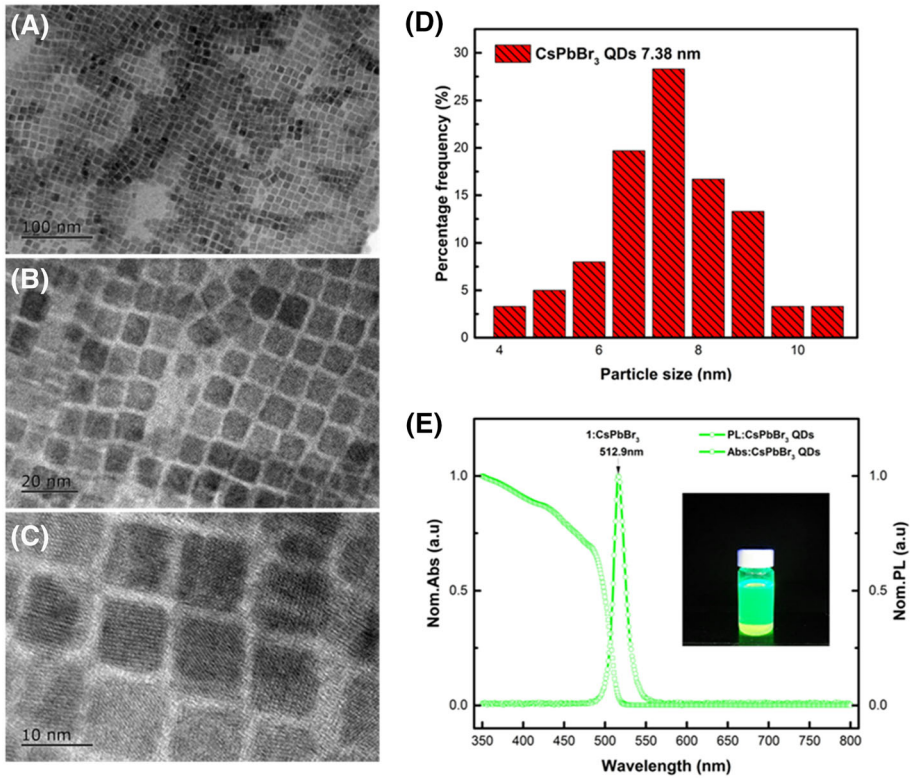

FIGURE 2 (A-C) High-resolution transmission electron microscope (HRTEM) images; (D) particle size distribution of $CsPbBr_3$ QDs and (E) PL and Abs spectra for $CsPbBr_3$ QDs [Colour figure can be viewed at wileyonlinelibrary.com]

QD/PPO solution. The QD mass concentration of the QD/PPO solutions are 0.625 to 10 mg/mL.

A total of two significant emission peaks existed in the RL spectra of $CsPbBr_3$ QDs/PPO solutions with different concentrations. A peak near 380 nm in the emission peak was identified as the RL peak of PPO. The peak position and values in the RL spectra of the C1 to C5 samples are illustrated in Figure 3. The QDs in C1 to C5 samples absorbed the fluorescence generated by PPO and converted it into the characteristic emission of QDs, leading

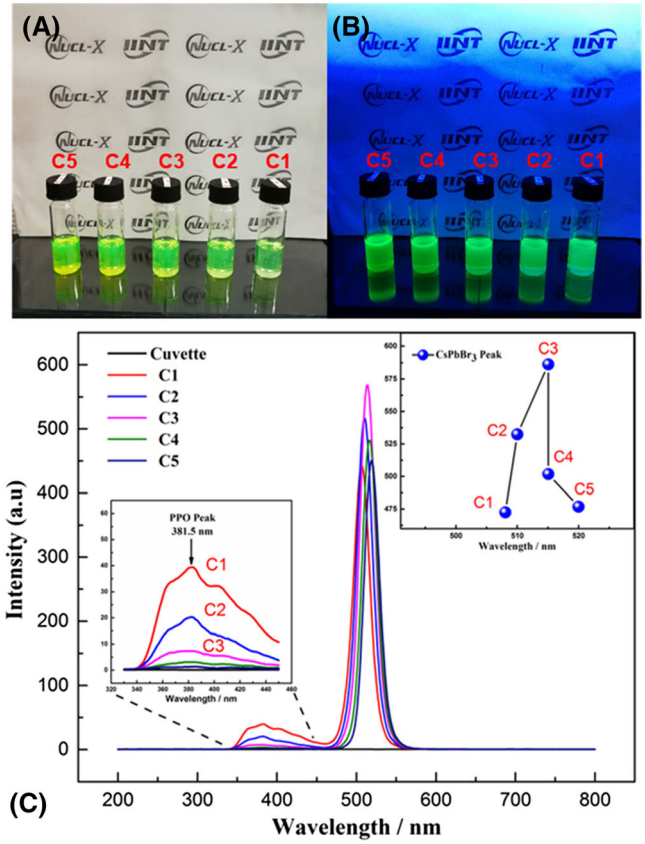

FIGURE 3 A, Different concentrations of $CsPbBr_3$ QDs/PPO solution in visible light: C1, 0.625 mg/mL; C2, 1.25 mg/mL; C3, 2.5 mg/mL; C4, 5 mg/mL; and C5, 10 mg/mL; B, different concentrations of $CsPbBr_3$ QDs/PPO solution under 365-nm UV lamps. C, The RL spectra of an empty cuvette and $CsPbBr_3$ QDs of different concentrations [Colour figure can be viewed at wileyonlinelibrary.com]

to the spectral regulation of the traditional liquid scintillators. The peak value of the $CsPbBr_3$ QDs/PPO solution increased first and then decreased with increasing QD concentration. This finding could be explained by the fact that the low QDs concentration cannot completely convert the fluorescence of the PPO and excess QD material could increase the absorbance of the $CsPbBr_3$ QDs/PPO solution. Finally, we determined that the optimum QD concentration in the QD/PPO solution is 2.5 mg/mL.

2.3 | Experimental methods

2.3.1 | PL and absorption spectra measurement

PL spectra of the QDs were obtained by using a fluorescence spectrometer (Cary Eclipse Spectrometer, Agilent Technologies Inc, Malaysia), and the UV/Vis absorption spectra were recorded using a UV/Vis spectrophotometer (Varian Cary 100, USA).

2.3.2 | HRTEM

A drop of $CsPbX_3$ QD solution was dispersed onto a Cu grid. HRTEM images were obtained on a Tecnai G2F30 S-TWIN instrument.

2.3.3 | Measurement of external quantum efficiency for GaAs devices

The external quantum efficiency curves of single-junction and triple-junction GaAs were obtained by solar cell quantum efficiency meter in Shanghai Institute of Space Power (Enlitech QE-R, Enli Technology Ltd, China).

2.3.4 | RL spectrum measurement

The X-ray source for RL spectrum measurement was an X-ray tube with Mo target and operated at 10 to 60 kV and 100 to 1000 μA. The RL spectrum was recorded at 200 to 1000 nm by using a fluorescence spectrophotometer. The voltage of the photomultiplier was set to 800 V, and the slit width of the monochromator was set to 20 nm.

2.3.5 | Measurement of the optical property of RL nuclear battery

Radioluminescence was imaged using an EMCCD camera (Andor iXon Ultra 888#BV, USA) equipped with a Canon EF 24 to 70 mm f/2.8 L II USM zoom lenses. The integration time for all images was set to 1 second. The image resolution set as 1024 × 1024 active pixels. The raw images were processed by subtracting the background image obtained under the same lighting conditions with turned off X-ray tube. All instruments were placed in the Faraday dark box during the experiments.

2.3.6 | Measurement of electrical property of RL nuclear battery

Current-voltage curve was measured by a dual-channel system source-meter instrument (Keithley 2636A, USA).

2.3.7 | X-ray tube energy spectrum measurement

The X-ray energy spectra of the X-ray tube (Shanghai KeyWay Electron Company Ltd. KYW900A, China) at different tube power levels (10-60 kV) were recorded using a hemispherical CdZnTe radiation probe (Shanxi Imdetek Company Ltd DT-01C1, China) and ORTEC

digital multichannel (ORTEC 572A/672, USA). X-ray beam was collimated by leads and hardened by 2-mm aluminum plates.

2.3.8 | In-situ polymerization of quantum dot thin films

A certain amount of 12-mL toluene solution and polystyrene (PS) were stirred uniformly by magnetic force at 65°C to 95°C, so that PMMA or PS monomer was completely dissolved and collocated into a stable sol. Then, it was vacuumed for 1.5 to 2.5 hours at 0.6 to 0.8 Mpa pressure to remove dissolved air gases from the sol and remained in dark environment for 1 day. The chemical properties of the sol system are stable. AIBN and perovskite quantum dots were added to the matrix material. Magnetic stirring at room temperature for 1.5 to 3 hours in a glove box insulated from oxygen and water makes the filler and matrix mix evenly. The stabilized sol was poured into the customized steel die. The dimension of the customized circular steel die was 10 mm × 5 mm in diameter. After vacuuming for 1 hour in a vacuum oven, low-temperature prepolymerization was carried out at 45°C for 42 hours, and then the temperature was gradually increased to 80°C for 3 to 5 hours. $CsPbBr_3$ quantum dot films with thickness of 24 to 342 μm were obtained after demolding. By adjusting the die size and postprocessing, different types of radiation sources and different sizes of radiation sources can be obtained. Figure 15 shows $CsPbBr_3$ quantum dot films prepared by in-situ polymerization.

3 | RESULT AND DISCUSSION

3.1 | Optical property of RL nuclear batteries

The RL images of different types of fluorescent materials (PPO, POPOP/PPO, $CsPbBr_3$ QDs, and $CsPbBr_3$ QD/PPO each at 5 mL and $CsPbBr_3$ QD concentration of 2.5 mg/mL) were obtained using an electron-multiplying charge-coupled devices (EMCCD) camera under different X-ray irradiation conditions (Figure 4).

The image resolution was set to 1024 × 1024 active pixels. The raw images were processed by subtracting a background image obtained under the same lighting conditions with the X-ray tube turned off. Andor Solis software (Solis Acquisition and Analysis Software) was used to obtain fluorescent photon counting and standard deviation data, and the gain effect was quantitatively analyzed. Reproducibility was checked by recording three consecutive images for each measurement, and the

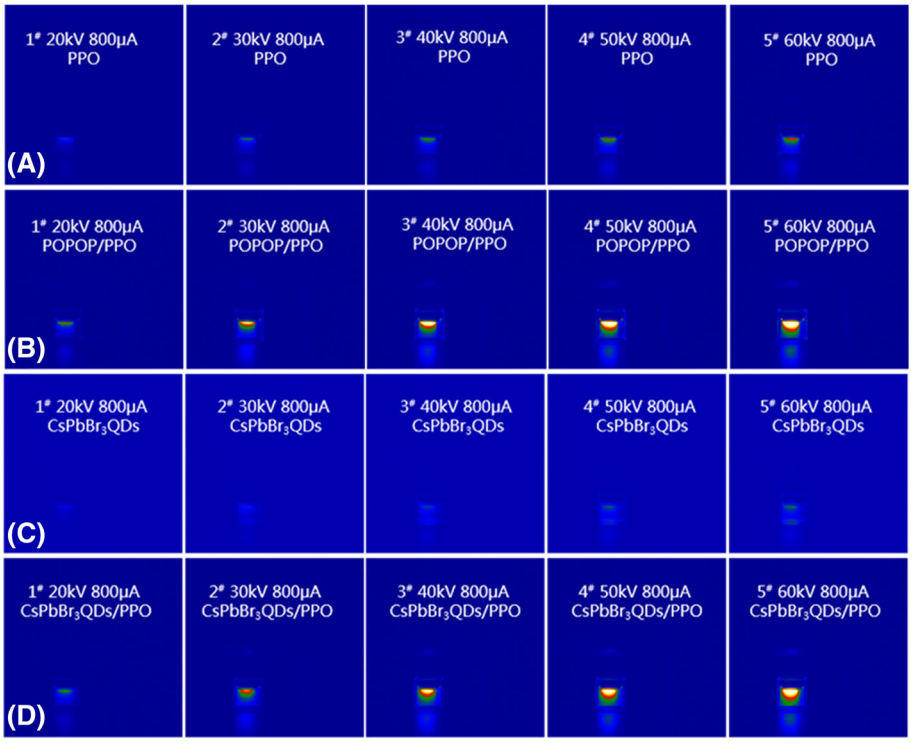

FIGURE 4 RL images of the samples A, PPO, (B) POPOP/PPO, C, $CsPbBr_3$ QDs, and D, $CsPbBr_3$ QDs/PPO) obtained by the EMCCD under different X-ray irradiation conditions. The tube voltage and the tube current were set at 20 to 60 kV and 800 μA [Colour figure can be viewed at wileyonlinelibrary.com]

standard deviations of each test result were calculated (Table S1-S4). The QD/PPO system captured by EMCCD produced significant higher counts than the PPO, QD, and POPOP/PPO systems. Figure 5 shows the count statistics of different solutions RL images under different radiation conditions.

Figure 5 shows that the counts of PPO RL images were significantly improved after using $CsPbBr_3$ QDs and POPOP as the wave-shifting agents. The fluorescence counts of QD/PPO and POPOP/PPO systems are higher than QD system or PPO system. The fluorescence count of the QD/PPO system is approximately 3.16 to 3.26 times higher than that of the PPO system. The count of the POPOP/PPO system is slightly higher than that of the QD/PPO system. The combination of POPOP and QDs as the wave-shifting agents combined with PPO effectively enhanced the counts of RL photons compared with the PPO systems. This enhancement consequently improved the output performance of the RL nuclear battery.

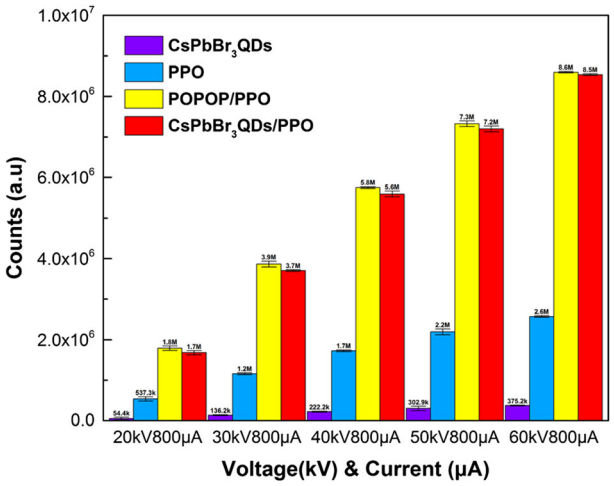

FIGURE 5 Count statistics of RL images of different solutions obtained by EMCCD under different radiation conditions [Colour figure can be viewed at wileyonlinelibrary.com]

3.2 | Selection of energy conversion devices

As a second-generation semiconductor, GaAs exhibits excellent characteristics such as wide band gap, high electron saturation drift velocity, direct-band-gap structures, a wide band and a small leakage current. Thus, GaAs is suitable for fabricating high-power, antiradiation, high-integrated electronic devices and circuits. To obtain improved electrical properties, we selected single and triple-junction GaAs as energy conversion devices of the RL nuclear battery.

These materials are widely used in solar cells, micro-electro-mechanical system (MEMS), and other devices and in various studies on nuclear batteries. Figure 6A,B, D,E shows the physical and structural diagrams of single and triple-junction GaAs. The efficient energy conversion area of the device used in this work was 10.1 mm × 11.1 mm. Figure 6C,F shows the external quantum efficiency of the different devices. Single-junction GaAs effectively converted the visible photons of 300 to 900 nm into electrical energy. The spectral range of triple-junction GaAs (200 to 2000 nm) is wider than that of single-junction GaAs, which is about 200 to 900 nm.

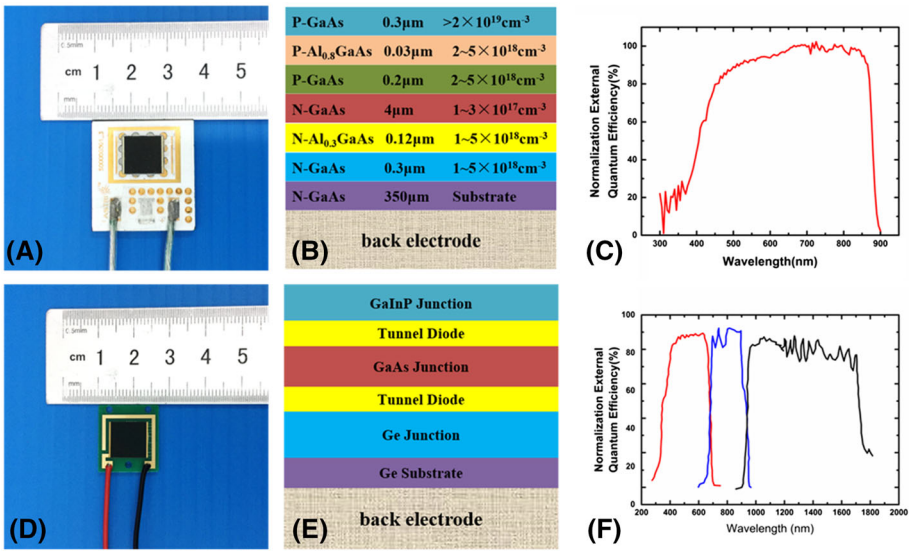

FIGURE 6 Two different energy conversion devices used in the experiment: A, single-junction GaAs; D, triple-junction GaAs; the structural representation of B, single-junction GaAs and E, triple-junction GaAs; the external quantum efficiency of C, single-junction GaAs and F, triple-junction GaAs [Colour figure can be viewed at wileyonlinelibrary.com]

3.3 | Electrical property of RL nuclear batteries

Single and triple-junction GaAs were used as energy conversion units to absorb the radioluminescence and produce an electrical output. The detailed structure of GaAs devices is shown in Figure 3. RL nuclear batteries are typically characterized through their electronic performance parameters such as short-circuit current (I_{sc}), open-circuit voltage (V_{oc}), maximum output power (P_{max}), and fill factor (FF). The physical and I-V curves are shown in Figure 7. The voltage and current at the maximum power point were denoted as I_{mp} and V_{mp}, respectively. P_{max} was calculated as follows:

$$P_{\max} = V_{mp} I_{mp} \tag{1}$$

$$FF = \frac{P_{\max}}{V_{oc} I_{sc}}. \tag{2}$$

At the I_{sc} and V_{oc} points, the power is zero, and P_{max} occurs between the two terms. FF is the ratio of P_{max} to the product of I_{sc} and V_{oc}.

The I-V curves of the RL nuclear battery with different fluorescence materials (PPO, POPOP/PPO, and $CsPbBr_3$ QD/PPO) and energy conversion devices (single and triple-junction GaAs) were measured by the experimental method presented in the subsequent section. The electrical properties of the RL nuclear batteries were compared.

The electrical properties of the QD/PPO and POPOP/PPO systems obtained from the I-V curves are significantly better than those of the PPO system. The dark current of the different devices was measured in a Faraday dark box with the X-ray tube turned off. The electrical properties of the QD/PPO system are superior to those of the POPOP/PPO system, in contrast to the characterization of previous optical properties. The reason for this conclusion is that the fluorescence photons of the QD/PPO system are more effectively absorbed and converted into electrical energy by GaAs devices compared with the fluorescent photons of the POPOP/PPO system. The values of I_{sc}, V_{oc}, P_{max}, and FF of the QD/PPO and PPO RL nuclear batteries were calculated based on the data in the I-V curves by using Equations 1 and 2.

Electrical property measurements are shown in Figure 8. The electrical properties of single and triple-junction GaAs changed in the same trend, that is QD/PPO system > POPOP/PPO system > PPO system. The electrical properties of QD/PPO and POPOP/PPO systems are superior to those of the PPO system, and the gain of the electrical properties of the RL batteries is remarkable with the addition of the two wave-shifting agents. This finding conforms to the test results of the optical properties and I-V curves.

QDs and POPOP can be used as wave-shifting agents to regulate the emission spectrum of PPO and gain the electrical properties of nuclear batteries. The scheme

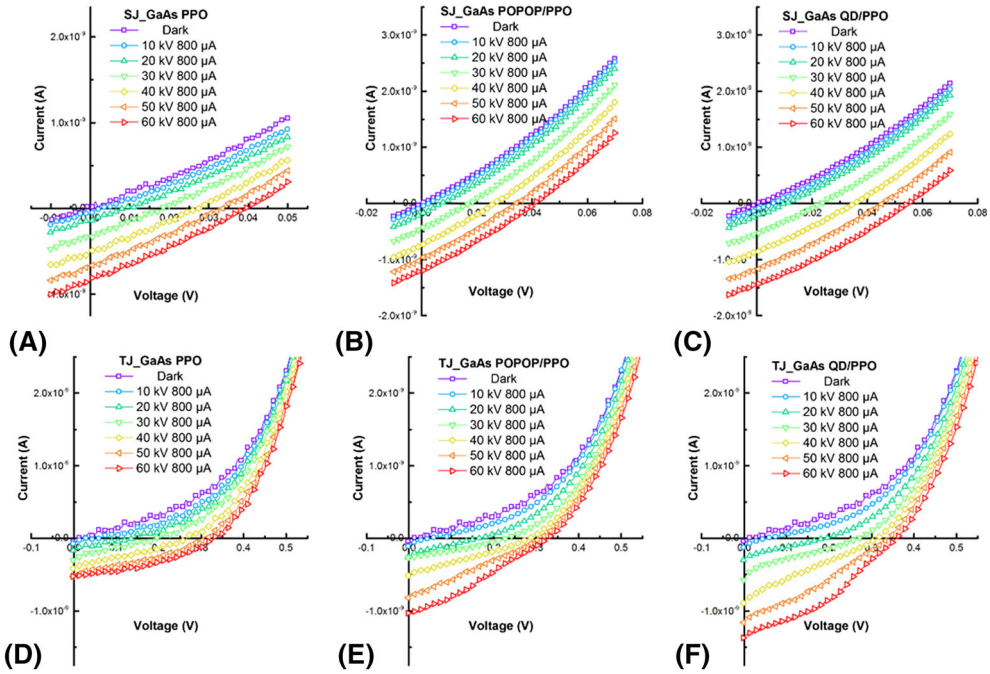

FIGURE 7 I-V characteristic curves of A, PPO, B, POPOP/PPO, and C, $CsPbBr_3$ QD/PPO RL nuclear batteries (single-junction GaAs as an energy conversion device); I-V characteristic curves of the D, PPO, E, POPOP/PPO, and F, $CsPbBr_3$ QD/PPO RL nuclear batteries (triple-junction GaAs as energy conversion device) [Colour figure can be viewed at wileyonlinelibrary.com]

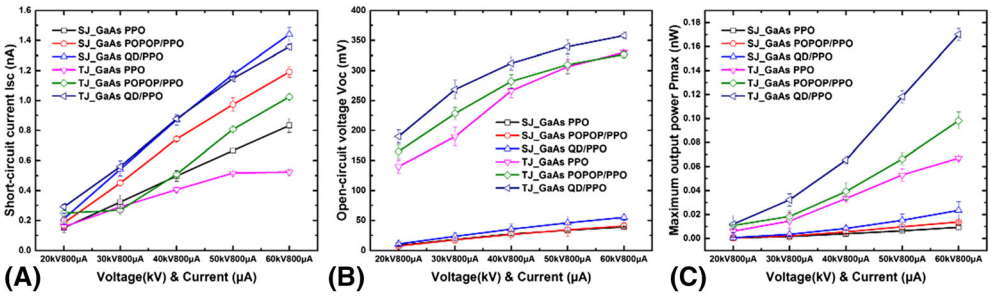

FIGURE 8 A, Short-circuit current (I_{sc}); B, open-circuit voltage (V_{oc}); and C, maximum output power (P_{max}) of the RL nuclear batteries [Colour figure can be viewed at wileyonlinelibrary.com]

has the same effect on single and triple-junction GaAs. The short-circuit current of single-junction GaAs is slightly higher than that of triple-junction GaAs; meanwhile, the open circuit voltage of triple-junction GaAs is much higher than that of single-junction GaAs. Thus, triple-junction GaAs exhibited better electrical performance than single-junction GaAs.

I_{sc}, V_{oc}, P_{max}, and FF are four core parameters for evaluating the electrical performance of batteries. The V_{oc}, I_{sc}, P_{max}, and FF of the PPO RL nuclear battery were all set at 1 for reference. Figure 9 shows the corresponding coefficients of the electrical parameters of the QD/PPO and POPOP/PPO nuclear RL batteries with respect to the PPO nuclear RL batteries.

Studies on nuclear batteries have mainly focused on improving electrical performance, and the maximum output power is the most concerned electrical parameter. The result of parameter calculation shows that the P_{max} gain of POPOP/PPO system is 1.42 to 1.80 times and 1.20 to 1.81 times compared with that of PPO system with single and triple-junction GaAs as energy conversion devices, respectively. The P_{max} gain of the QD/PPO system is 1.91 to 2.53 times and 2.03 to 2.51 times that of the PPO system with single and triple-junction GaAs as energy conversion devices, respectively. For the RL nuclear battery, the addition of QDs led to the excellent optical and electrical properties, and the gain of electrical properties is also better than that of the traditional wave-shifting agent POPOP.

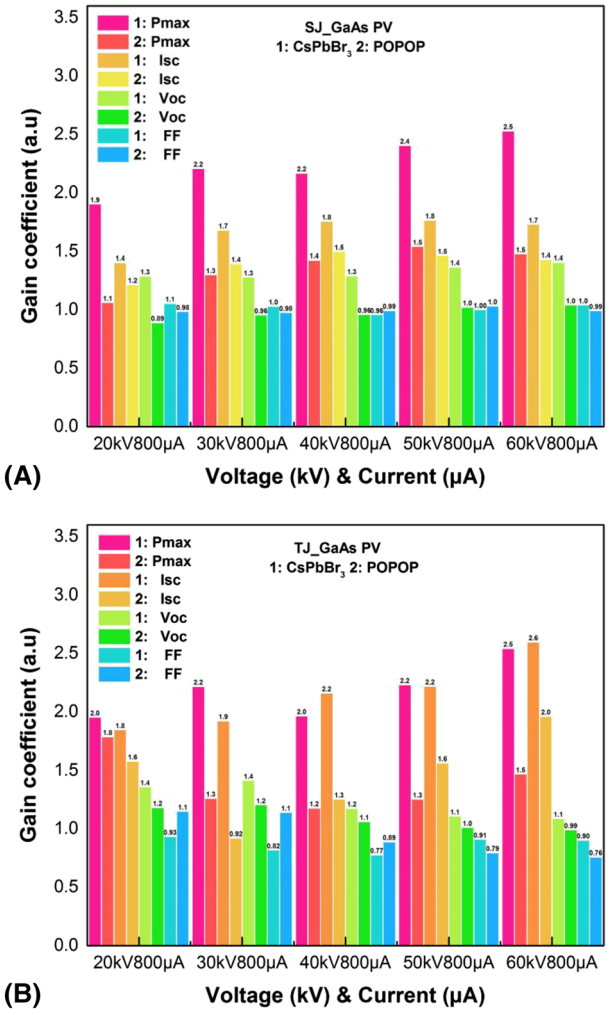

FIGURE 9 Gain coefficients of V_{oc}, I_{sc}, P_{max}, and FF of the QD/PPO and POPOP/PPO RL nuclear batteries A, single-junction GaAs and B, triple-junction GaAs as energy conversion devices (PPO RL nuclear battery as reference) [Colour figure can be viewed at wileyonlinelibrary.com]

3.4 | Calculation of spectral matching factor (SMF)

The normalized RL spectra of PPO, POPOP/PPO, and QD/PPO systems were recorded under different X-ray irradiation conditions (Figure 10). The spectral compatibility of the QD/PPO, POPOP/PPO, and PPO radioluminescence with the spectral sensitivity of various optical photon detectors (single and triple-junction GaAs) was estimated using SMF[24]:

$$SMF = \frac{\int S_p(\lambda) S_D(\lambda) d\lambda}{\int S_p(\lambda) d\lambda} \quad (3)$$

where S_P is the RL spectra of QD/PPO, POPOP/PPO, and PPO, S_D is the spectral sensitivity of the GaAs devices,

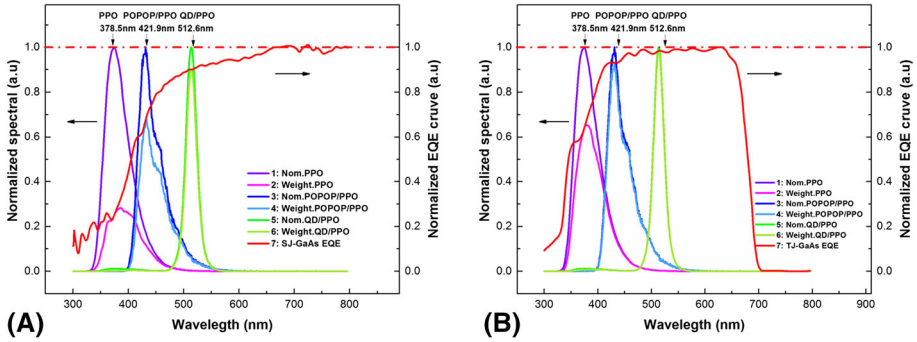

FIGURE 10 A, Normalized RL spectra of PPO, POPOP/PPO, and $CsPbBr_3$ QD/PPO and the external quantum efficiency curve of single-junction GaAs and B, normalized RL spectra of PPO, POPOP/PPO, and $CsPbBr_3$ QD/PPO and the external quantum efficiency of triple-junction GaAs [Colour figure can be viewed at wileyonlinelibrary.com]

and λ denotes the wavelength of the radioluminescence. The above experimental method was used to characterize the RL spectra of different fluorescent materials to obtain normalized RL spectra. The external quantum efficiency curve of the GaAs devices was obtained from the test.

The SMFs of the PPO, POPOP/PPO, and $CsPbBr_3$ QD/PPO materials were calculated using the data in Figure 10 and Equation (3). The FWHM and peak RL spectra of different fluorescent materials and the SMF for GaAs are shown in Table 1.

Based on the normalized RL spectra, both types of wave-shifting agents ($CsPbBr_3$ QD and POPOP) effectively absorbed the radioluminescence generated by PPO under different X-ray irradiation conditions. The emission wavelengths of the QD/PPO and POPOP/PPO systems were determined by the characteristic emission wavelengths of QDs and POPOP.

The selected $CsPbBr_3$ QD can be used as a wave-shifting agent to obtain a more suitable emission spectrum and a narrower FHWM. The RL emission spectra of QD/PPO systems are determined by the type of QDs. For GaAs devices, the SMF of the QD/PPO system is almost two times the SMF of the PPO system and is superior to the POPOP/PPO system, which is considered to be the main reason for the significant improvement in optical and electrical properties.

TABLE 1 The QD/PPO and PPO SMF of GaAs devices

SMF	Single-Junction GaAs, %	Triple-Junction GaAs, %	Peak, nm	FHWM, nm
PPO	42.48	36.76	378.5	54.2
POPOP/PPO	91.74	88.34	421.9	52.2
$CsPbBr_3$ QD/PPO	95.44	92.38	512.8	10.1

3.5 | RL nuclear battery based on QD/PPO and liquid radioactive source by MCNP simulation

3.5.1 | Radioactive source selection of radioluminescenct nuclear battery

The specific parameters of the X-ray tube are shown in Table 2. The obtained X-ray spectrum information and the test system are shown in Figure 11.

The X-ray spectra of the X-ray tube at different tube powers (10-60 kV) were recorded using a CdZnTe radiation probe and ORTEC digital multichannel.

The X-ray spectra show that adjusting the X-ray tube voltage can regulate the emitted X-ray energy and can be used for equivalent different low-energy X-ray sources. In recent years, an increasing number of GaAs ^{55}Fe nuclear batteries have been developed using low-energy ^{55}Fe radioisotope X-ray sources and GaAs devices.[18,21] The average energy of the X-ray tube is close to that of natural radionuclide ^{55}Fe with the voltage of 10 kV. The activity of the X-ray tube was converted into 3.0755×10^{11} Bq for the tube current of 800 μA which is equivalent to the natural radionuclide ^{55}Fe of 8.3123 Ci.

3.5.2 | Monte Carlo simulation of RL nuclear battery

The computational software used in theoretical research is Monte Carlo N particle general code 6 (MCNP 6.1). The physical model of MCNP can be divided into three types: solid cylinder radiation source, liquid radiation source, and X-ray external radiation source (Figure 12). The size of the three models was set as 3 cm × 3 cm × 6 cm cuvette with a wall thickness of 2 mm, which is consistent with the experiments. After optimizing the

TABLE 2 Specific parameters of the X-ray tube

Anode Voltage	Anode Current	Maximum Power	Filament Voltage	Filament Characteristic
60 kV	0-1 mA	65 W	2.0 V	$I_f \approx 1.7$ A
Thickness of beryllium window	Target angle	Focus spot size	Grounded mode	Target
200 μm	10°	0.1 mm × 0.1 mm	Grounded cathode	Molybdenum

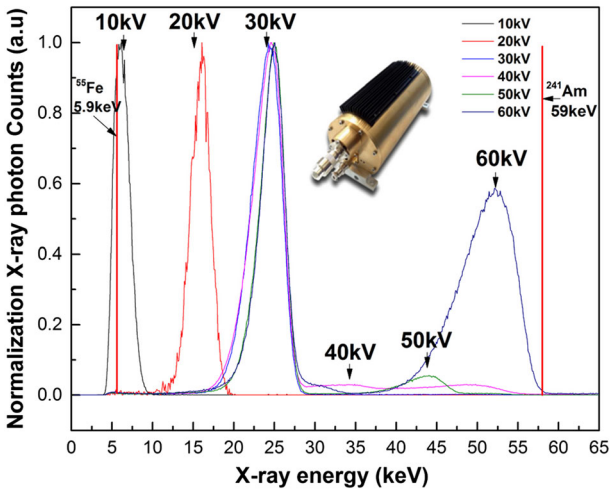

FIGURE 11 Energy spectrum of X-ray tube obtained by CdZnTe detector [Colour figure can be viewed at wileyonlinelibrary.com]

concentration of QDs, the fluorescence material selected in the three models was QD/PPO.

The solid source model can be described as a cylindrical radiation source with various physical parameters placed in the center of a cube. The height of the radiation source is set to 6 cm, and the radius of the cylindrical radiation source are set as 0.1, 0.2, 0.3, 0.4, or 0.5 cm, respectively. A model of a liquid source can be described as a liquid source of the same mass with a solid source diffusing in a cube of the same size. ^{55}Fe was used as the excitation source in the solid and liquid source models, and the X-ray tube energy spectrum detected by CdZnTe was used as the excitation source in the X-ray external radiation source model.

Figure 12A shows a physical model of X ray external irradiation, consisting of a colorimetric dish and a liquid fluorescent material. Figure 12B presents a physical

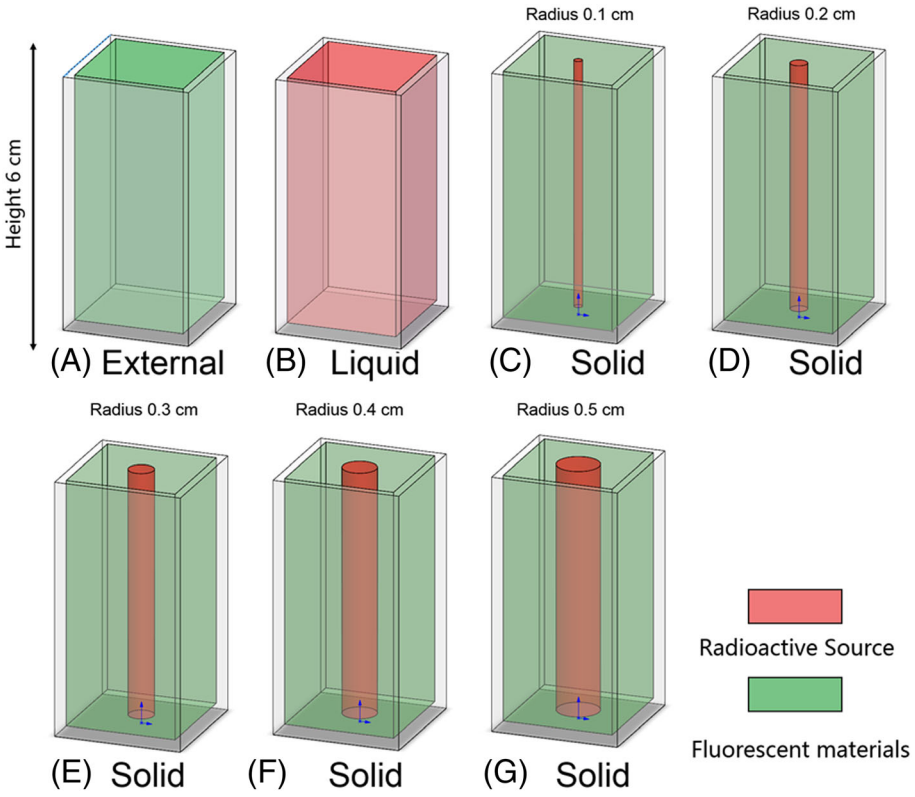

FIGURE 12 The physical model for the MCNP simulation [Colour figure can be viewed at wileyonlinelibrary.com]

model of a liquid radioactive source consisting of a colorimetric dish and a mixed liquid (liquid radioactive source ^{55}Fe and liquid fluorescent material). Figure 12C-G demonstrates a physical model of solid radioactive sources consisting of a colorimetric dish and a cylinder radioactive source ^{55}Fe. In diverse physical models, the absorbed dose and energy deposition in fluorescent materials are provided in Table 3. The specific values of the absorbed dose of a cylindrical source and the fluorescent material in the solid source model are shown in Table S5. The number of simulated particles was 1×10^7, and the errors were all less than 0.03%.

In the solid source model, the absorbed dose and energy deposition of fluorescent materials only accounted for 0.02% to 2.65% of the total absorbed dose and energy deposition, because the cylindrical source itself has a significant shielding effect on the low-energy X-ray produced by ^{55}Fe. The results of MCNP simulation show that the liquid radiation source combined with liquid fluorescent material exhibits advantages over the traditional solid radiation source for low-energy X-ray source ^{55}Fe. The absorbed dose and energy deposition calculated by the X-ray external radiation model are 2.8994×10^{-27} Gy and 1.5103×10^{-25} J, respectively. In previous studies, on RL nuclear battery, the energy deposition in fluorescent materials is proportional to the P_{max} and shows a linear relationship within a certain range.[15,19] Therefore, we can estimate the electrical output performance of various physical models through the energy deposition calculated by various physical models.

Figure 13A,B shows the P_{max} of different physical models with single-junction GaAs and three-junction GaAs as devices, respectively. Sequence 1 in Figure 13 is the electrical output of the X-ray external source model obtained by previous electrical experiments. Sequences 2 to 5 and Sequences 6 to 11 are the solid and liquid source models, respectively. The results show that the energy deposition of both solid and liquid radiation source models is significantly better than that of X-ray radiation source models. Furthermore, the energy deposition in the liquid source model is significantly better than that in the solid source model because the liquid source ^{55}Fe and the liquid fluorescent material can be fully contacted and the radiation source self-absorption is significantly less than that in the solid column model. The P_{max} values of liquid radiation source model with single and three-junction GaAs as devices are 62.68 nW and 1.15 μW, respectively.

3.5.3 | ^{63}Ni/CsPbBr$_3$ QDs/PPO/GaAs RL nuclear battery

$CsPbBr_3$ QDs with green emission are selected for perovskite quantum dots. The reason is that $CsPbBr_3$ QDs have the highest fluorescence quantum efficiency and the emission spectrum of $CsPbBr_3$ QDs is located near the peak wavelength of the external quantum efficiency curve of GaAs photovoltaic semiconductor. Selecting $CsPbBr_3$ QDs is conducive to obtaining better electrical

TABLE 3 Radiation absorbed dose and energy deposition of different source

Solid Source	Absorbed Dose, Gy	Energy Deposition, J	Liquid Source	Absorbed Dose, Gy	Energy Deposition, J
1	1.82E − 29	9.81E − 28	1	1.10E − 26	5.88E − 25
2	2.72E − 29	1.45E − 27	2	1.28E − 26	7.35E − 25
3	3.87E − 29	2.02E − 27	3	1.49E − 26	9.48E − 25
4	6.11E − 29	3.11E − 27	4	1.63E − 26	1.18E − 24
5	1.18E − 28	5.83E − 27	5	1.63E − 26	1.38E − 24

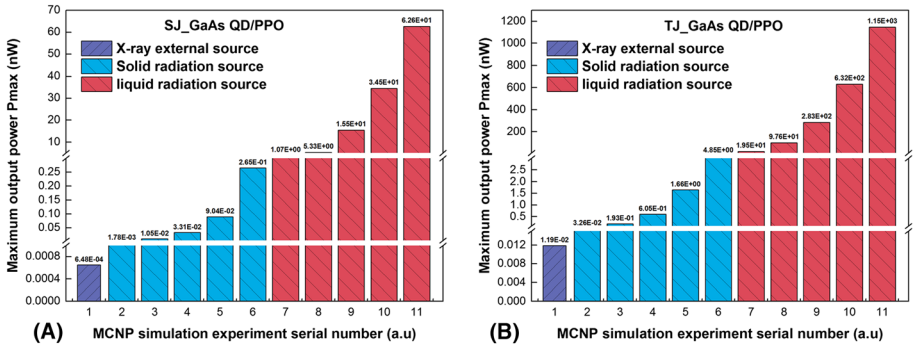

FIGURE 13 P_{max} of the three type models [Colour figure can be viewed at wileyonlinelibrary.com]

properties. $CsPbBr_3$ QDs/PPO films with thickness ranging from 24 to 342 μm were prepared by in situ polymerization. The *I-V* curves of PPO and $CsPbBr_3$ QD/PPO radioluminescence nuclear battery were recorded with an electrical performance test system at ^{63}Ni radiation source, as shown in Figure 14.

Radioluminescence emission spectra of $CsPbBr_3$ QDs/PPO films with one to four thickness of 24.5, 44.8, 62.1, and 85.1 μm, respectively, are shown in Figure 14. $CsPbBr_3$ QDs regulate the irradiation fluorescence of PPO to a certain extent. Because the energy of ^{63}Ni radiation source is low, the depth of radiation particles penetrating the material is shallow. The *I-V* curves of ^{63}Ni/QD/PPO radioluminescenct nuclear battery show that the electrical performance of the cell prepared by $CsPbBr_3$ QDs/PPO film with thickness of 24.5 μm is better than that of the PPO radioluminescenct nuclear battery, and the maximum output power is 1.38 pW.

3.5.4 | Application prospect

In this paper, tunable properties of $CsPbBr_3$ QDs materials are used to improve the adaptability of traditional fluorescent materials with different device. All-inorganic perovskite quantum dots enable full-spectrum regulation of the visible light band by changing the composition and particle size of the quantum dots. Physical diagrams and normalized radiation emission spectrum of all-inorganic perovskite quantum dots of different compositions are shown in Figure 15.

All-inorganic perovskite quantum dots enable spectral control in the visible range to adapt to devices (PMT photomultipliers, Si-PD silicon photodiodes, CCD charge-coupled devices, etc.) that respond to different spectral ranges. The research ideas of using quantum dot fluorescent materials to improve the adaptability of optoelectronic devices and emission spectra have certain

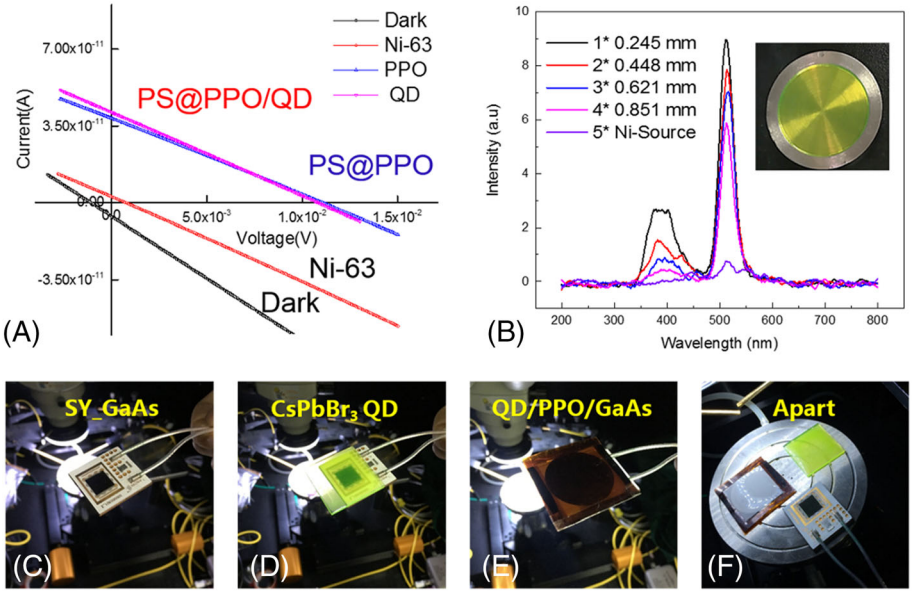

FIGURE 14 A, Emission spectra of QD/PPO films under ^{63}Ni radiation source, B, *I-V* curves of ^{63}Ni/QD/PPO RL nuclear battery, and (C-)F ^{63}Ni/QD/PPO RL nuclear battery [Colour figure can be viewed at wileyonlinelibrary.com]

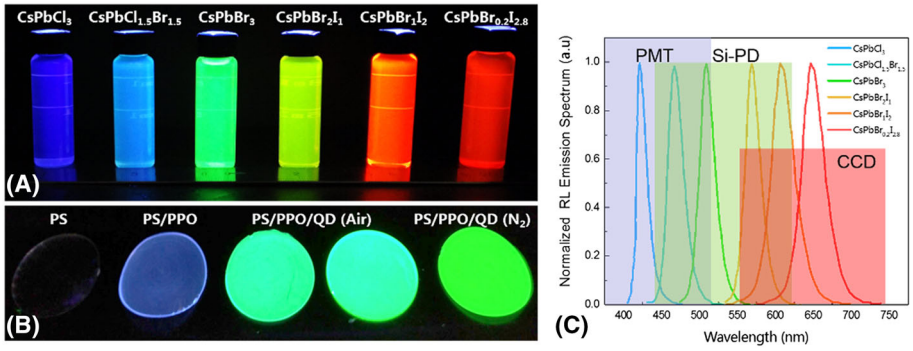

FIGURE 15 A, Physical diagram of all-inorganic perovskite $CsPbX_3$ (Cl, Br, I) QDs. B, Physical diagram of $CsPbX_3$ QDs films. C, RL spectra of all-inorganic perovskite $CsPbX_3$ (Cl, Br, I) QDs [Colour figure can be viewed at wileyonlinelibrary.com]

reference significance and application value in radiation sensors, nuclear batteries, radiation detectors, and nuclear medicine imaging.

4 | CONCLUSIONS

The size and emission wavelengths of $CsPbBr_3$ QDs synthesized by hot-injection method are 7.38 and 512.9 nm, respectively. The fluorescence emission spectra of QD/PPO were characterized. The optimum concentrations of PPO, POPOP/PPO, and QD/PPO systems was 2, 0.2, and 2.5 mg/mL, respectively, according to RL intensity.

The fluorescence counts significantly increased in the PPO system after using the wave-shifting agents. The EMCCD count in the QD/PPO and POPOPO/PPO systems increased by approximately 3.30 to 3.35 times over the PPO systems. Moreover, the POPOP/PPO systems have excellent optical properties.

The electrical properties of the QD/PPO and POPOP/PPO RL nuclear batteries significantly improved. The P_{max} values of the POPOP/PPO system are 1.42 to 1.80 and 1.20 to 1.81 times that of the PPO system, respectively, with single and triple-junction GaAs as the energy conversion devices. The P_{max} values of the QD/PPO system are 1.91 to 2.53 times and 2.03 to 2.51 times of the PPO system, respectively, with GaAs devices. Hence, the electrical property of the QD/PPO system is better than that of POPOP/PPO system.

Three radiation source models were simulated by the Monte Carlo method. Based on the simulation and experimental results, liquid fluorescent materials combined with liquid radiation source are an effective scheme to significantly enhance the energy deposition in fluorescent materials. This work provides a theoretical basis for the development of RL nuclear cells based on liquid fluorescent materials and liquid radioactive sources. The results also verify that the application of liquid fluorescent materials in nuclear battery.

$CsPbBr_3$ QDs can be used as a wave-shifting agent to control the emission spectrum of PPO and significantly improve the overall output performance of the RL nuclear battery. The strategy of using all-inorganic perovskite QDs as wave-shifting agents to regulate the emission spectrum of traditional fluorescent materials has potential applications in the fields of RL nuclear battery, nuclear detection, and nuclear medicine imaging technology.

ACKNOWLEDGEMENTS

The authors would like to acknowledge the support of the National Natural Science Foundation of China (Grant No. 11675076) and the Shanghai Aerospace Science and Technology Innovation Project (Grant No. SAST2016112).

ORCID

Xiaobin Tang https://orcid.org/0000-0003-3308-0468

REFERENCES

1. Saotome Y, Iwazaki H. Superplastic backward microextrusion of microparts for micro-electro-mechanical systems. *J Mater Process Technol*. 2001;119(1-3):307-311.
2. Schmidt G, Dudzinski L, Sutliff T. Radioisotope power: a key technology for deep space exploration. In: *6th International Energy Conversion Engineering Conference (IECEC)*, Cleveland, Ohio, 2011:5640.
3. Walton R, Anthony C, Ward M, Metje N, Chapman DN. Radioisotopic battery and capacitor system for powering wireless sensor networks. *Sensors and Actuators a: Physical*. 2013;203:405-412.
4. Qiao DY, Chen XJ, Ren Y, Yuan WZ. A micro nuclear battery based on SiC schottky barrier diode. *Journal of Microelectromechanical Systems*. 2011;20(3):685-690.
5. San H, Yao S, Wang X, Cheng Z, Chen X. Design and simulation of GaN based Schottky betavoltaic nuclear micro-battery. *Appl Radiat Isot*. 2013;80:17-22.
6. Theirrattanakul S, Prelas M. A methodology for efficiency optimization of betavoltaic cell design using an isotropic planar source having an energy dependent beta particle distribution. *Appl Radiat Isot*. 2017;127:41-46.
7. Prelas MA, Weaver CL, Watermann ML, Schott RJ, Wisniewski DA. A review of nuclear batteries. *Progr Nucl Energ*. 2014;75:117-148.
8. Xu ZH, Liu YP, Zhang ZR, et al. Enhanced radioluminescent nuclear battery by optimizing structural design of the phosphor layer. *International Journal of Energy Research*. 2018;42(4):1729-1737.
9. Prelas MA, Tchouaso MT. High efficiency dual-cycle conversion system using Kr-85. *Appl Radiat Isot*. 2018;139:70-80.
10. Kim T, Lee N, Jung HK, Kim JH. Enhancement of energy performance in betavoltaic cells by optimizing self-absorption of beta particles. *International Journal of Energy Research*. 2016;40(4):522-528.
11. Sychov M, Kavetsky A, Yakubova G, et al. Alpha indirect conversion radioisotope power source. *Appl Radiat Isot*. 2008;66(2):173-177.
12. Alam TR, Spencer MG, Prelas MA, Pierson MA. Design and optimization of radioisotope sources for betavoltaic batteries. *International Journal of Energy Research*. 2018;42(7):2564-2573.
13. Russo J, Litz M, Ray W, Smith B, Moyers R. A radioluminescent nuclear battery using volumetric configuration: ^{63}Ni solution/ZnS: Cu, Al/InGaP. *Appl Radiat Isot*. 2017;130:66-74.
14. Butera S, Lioliou G, Barnett AM. Gallium arsenide ^{55}Fe X-ray-photovoltaic battery. *J Appl Phys*. 2016;119(6):064504.

15. Lu M, Zhang GG, Fu K, Yu GH, Su D, Hu JF. Gallium nitride schottky betavoltaic nuclear batteries. *Energ Conver Manage*. 2011;52(4):1955-1958.
16. Butera S, Lioliou G, Krysa AB, Barnett AM. Al0.52In0.48P ^{55}Fe x-ray-photovoltaic battery. *J Phys D Appl Phys*. 2016;49(35):355601.
17. Tang XB, Hong L, Xu ZH, Liu YP, Chen D. Temperature effect of a radioluminescent nuclear battery based on ^{147}Pm/ZnS:Cu/GaAs. *Appl Radiat Isot*. 2015;97:118-124.
18. Chen W, Tang XB, Liu YP, et al. Novel radioluminescent nuclear battery: spectral regulation of perovskite quantum dots. *International Journal of Energy Research*. 2018;42(7):2507-2517.
19. Butera S, Lioliou G, Barnett AM. Temperature effects on gallium arsenide ^{63}Ni betavoltaic cell. *Appl Radiat Isot*. 2017;125:42-47.
20. Swarnkar A, Chulliyil R, Ravi VK, Irfanullah M, Chowdhury A, Nag A. Colloidal $CsPbBr_3$ perovskite nanocrystals: luminescence beyond traditional quantum dots. *Angew Chem Int Ed*. 2015;54(51):15424-15428.
21. Nikolopoulos D, Valais I, Michail C, et al. Radioluminescence properties of the CdSe/ZnS quantum dot nanocrystals with analysis of long-memory trends. *Radiat Meas*. 2016;92:19-31.
22. Chen W, Liu Y, Yuan Z, et al. X-ray radioluminescence effect of all-inorganic halide perovskite $CsPbBr_3$ quantum dots. *J Radioanal Nucl Chem*. 2017;134(3):2327-2337.
23. Palazon F, Akkerman QA, Prato M, Manna L. X-ray lithography on perovskite nanocrystals films: from patterning with anion-exchange reactions to enhanced stability in air and water. *ACS Nano*. 2016;10(1):1224-1230.
24. Valais I, Nikolopoulos D, Kalivas N, et al. A systematic study of the performance of the CsI:Tl single-crystal scintillator under X-ray excitation. *Nucl Instrum Methods Phys Res, Sect a*. 2007;571(1-2):343-345.

SUPPORTING INFORMATION

Additional supporting information may be found online in the Supporting Information section at the end of the article.

How to cite this article: Chen W, Tang X, Liu Y, et al. Radioluminescent nuclear battery containing $CsPbBr_3$ quantum dots: Application of a novel wave-shifting agent. *Int J Energy Res*. 2019;43:4520–4533. https://doi.org/10.1002/er.4580